

# Nonrigid registration with free-form deformation model of multilevel uniform cubic B-splines: application to image registration and distortion correction of spectral image cubes

Timo Eckhard,\* Jia Eckhard, Eva M. Valero, and Juan Luis Nieves

Optics Department, University of Granada, C. Fuentenueva s/n, 18071 Granada, Spain

\*Corresponding author: timo.eckhard@gmx.com

Received 31 January 2014; accepted 25 April 2014;  
posted 7 May 2014 (Doc. ID 205504); published 10 June 2014

In spectral imaging, spatial and spectral information of an image scene are combined. There exist several technologies that allow the acquisition of this kind of data. Depending on the optical components used in the spectral imaging systems, misalignment between image channels can occur. Further, the projection of some systems deviates from that of a perfect optical lens system enough that a distortion of scene content in the images becomes apparent to the observer. Correcting distortion and misalignment can be complicated for spectral image data if they are different at each image channel. In this work, we propose an image registration and distortion correction scheme for spectral image cubes that is based on a free-form deformation model of uniform cubic B-splines with multilevel grid refinement. This scheme is adaptive with respect to image size, degree of misalignment, and degree of distortion, and in that sense is superior to previous approaches. We support our proposed scheme with empirical data from a Bragg-grating-based hyperspectral imager, for which a registration accuracy of approximately one pixel was achieved. © 2014 Optical Society of America

*OCIS codes:* (110.4234) Multispectral and hyperspectral imaging; (100.2980) Image enhancement; (150.1488) Calibration.

<http://dx.doi.org/10.1364/AO.53.003764>

## 1. Introduction

Multi- or hyper-spectral image acquisition techniques have drawn increasing attention in both industry and science in recent years [1–3]. A multi- or hyper-spectral image cube combines spatial and spectral information of the scene content [4]. Usually, a spectral image cube can be considered as a stack of images with varying spectral content. The distinction between multi- and hyper-spectral image cubes is often based on the number of spectral channels acquired by the system. However, for our work this distinction is

not critical, and in what follows we therefore simply refer to spectral image cubes or spectral data.

In an optimal spectral imaging system, the image content is free of spatial distortion and image misalignment among image channels. A correct alignment means that pixels in each image channel correspond to the same physical region of the scene being imaged [5]. An image free of spatial distortion is that produced by an optimal rectilinear lens system, for which scene content is projected without deformation on the image sensor.

However, in real imaging systems, image distortion is always present to some extent due to imperfect optical components. The most common forms of distortion are radially symmetric and related to the symmetry properties of the lens system. If image

distortion varies among image channels, it ultimately leads to image misalignment. Spatial misalignment in multichannel image data can also be due to many other reasons. For instance, spectral images acquired by rotating different color glass filters in front of a camera lens [6] cause pixel misalignment among spectral channels. This is mostly due to the mechanical mounting of the filters in the wheel, causing variation in image projection for individual filters [7]. Another source of misalignment is linked to the presence of uncorrected transversal chromatic aberrations, which causes a deviation of lens magnification that depends on the wavelength of light that passes the optical system [7,8]. Also, the usage of different optical components to acquire various spectral image channels can cause misalignment. Multisensor systems [9] or the multiple Bragg-grating-based hyperspectral imager (Hyperspectral Camera V-EOS by Photon etc.) [10] considered in this work are examples in which this applies.

It becomes clear that image distortion and image misalignment are closely linked when it comes to multichannel image data. A review of literature reveals a large variety of potential solutions for both problems. For instance, radial and tangential distortion can be modeled and corrected by Brown's distortion model [11,12]. Misalignment can be corrected by image registration, for which Zitova and Flusser give an extensive overview [13]. However, a solution that accounts for both effects is preferable.

In this work, we concentrate on a method that belongs to the category of elastic registration models based on B-splines [14]. The free-form deformation model of multilevel uniform cubic B-splines used in this paper can correct image misalignment and account for image distortion of arbitrary kind. Model parameters are obtained in a fitting process that is performed once for a calibration image scene. Once obtained, the model can be applied to correct arbitrary spectral images captured in similar conditions. The approach is adaptive with respect to image size, degree of misalignment, and degree of distortion, which is superior to previous approaches applied to the same problem. A detailed comparison of this approach with a related work by Špiclin *et al.* [15] can be found in Section 4.

This paper is organized as follows. Section 2 introduces the image registration model for spectral image data proposed in this work. Real image data, acquired from a calibration scene, are used to obtain the model parameters. The model is then applied to a test scene, and registration performance is evaluated analytically. This part of the work is described in Section 3. In Section 5, we discuss our findings and summarize the most relevant conclusions extracted from the results.

## 2. Spectral Image Registration Model

Let  $\mathbf{C}$  be an unregistered and distorted spectral image cube, which contains a sequence of image data matrices  $\{I_\lambda \in \mathbb{M}(r, c) | \lambda = 1, 2, \dots, w\}$ , where  $\mathbb{M}(r, c)$  denotes the set of  $r \times c$  matrices, with  $r \times c$  being

the image resolution and  $w$  the number of spectral channels. Further, let  $\mathbf{C}_0$  be the corresponding reference spectral image cube  $\{I_{\lambda 0} \in \mathbb{M}(r, c) | \lambda = 1, 2, \dots, w\}$ , whose images are spatially aligned and free of distortion. The domain of image coordinates is  $\Omega = \{(x, y) \in \mathbb{N}^2 | 0 \leq x \leq r - 1, 0 \leq y \leq c - 1\}$ .

Registration and distortion correction is the process of aligning each image  $I_\lambda$  spatially to its reference image  $I_{\lambda 0}$ . The problem to be solved is finding a displacement matrix set  $\mathbf{D} = \{Z_\lambda = [z_\lambda(x, y)]_{r \times c} | (x, y) \in \Omega, \lambda = 1, 2, \dots, w\}$ , containing displacement vector fields  $Z_\lambda$  for every image channel, such that  $I_\lambda((x, y) + z_\lambda(x, y)) = I_{\lambda 0}(x, y)$ .

Without loss of generality we consider further only the registration and distortion correction of one arbitrary spectral image channel  $I$  to its reference image  $I_0$ . The corresponding displacement vector field  $Z$  can be decomposed into horizontal and vertical displacement fields  $Z_u = [z_u(x, y)]_{r \times c}$  and  $Z_v = [z_v(x, y)]_{r \times c}$ , such that

$$I((x + z_u(x, y), y + z_v(x, y))) = I_0(x, y). \quad (1)$$

We assume horizontal and vertical displacements to be independent and therefore illustrate in what follows only the case of horizontal displacement.

### A. Displacement Representation by Uniform Cubic B-Splines Modeled Surface

The surface characterizing a displacement field can be described in parametric form as  $\mathbf{Q}(s, t) = (x(s, t), y(s, t), z(s, t))$ , with  $(s, t)$  being the surface parameters in the range  $[0, 1]$ , and  $z$  being the displacement at pixel position  $(x, y)$ . We model the surface using uniform cubic B-splines [14]. The projection of the surface on the  $xy$  plane is divided into  $n_r \times n_c$  patches of size  $\delta \times \delta$ , and the surface  $\mathbf{Q}$  is divided into  $n_r \times n_c$  subsurfaces  $\{\mathbf{Q}_{\mu\nu} | \mu = 0, 1, \dots, n_r - 1, \nu = 0, 1, \dots, n_c - 1\}$ . Each subsurface is controlled by  $4 \times 4$  B-spline control points. The whole surface  $\mathbf{Q}$  is controlled by  $(n_r + 3) \times (n_c + 3)$  control points  $\{\mathbf{p}_{ij} = (x_{ij}, y_{ij}, z_{ij}) | x_{ij} = (i - 1) \cdot \delta, y_{ij} = (j - 1) \cdot \delta, i = 0, 1, \dots, n_r + 2, j = 0, 1, \dots, n_c + 2\}$ , located on a uniform grid of spacing  $\delta \times \delta$ , where  $(x_{ij}, y_{ij})$  are known spatial coordinates. Note that we set the coordinate of the top-left pixel of the image domain  $\Omega$  as  $(0, 0)$ , so we allow negative values of the coordinates whose spatial location is beyond this point in upward and leftward directions.

Figure 1(a) illustrates an example of a surface that consists of  $3 \times 3$  subsurfaces. These subsurfaces are controlled by  $6 \times 6$  control points located on a uniform grid [illustrated in Fig. 1(b)].

Each subsurface  $\mathbf{Q}_{\mu\nu}$ , modeled by uniform cubic B-splines, can be represented as

$$\begin{aligned} \mathbf{Q}_{\mu\nu}(s, t) &= \sum_{i=0}^3 \sum_{j=0}^3 \mathbf{p}_{\mu+i, \nu+j} B_i(s) B_j(t) \\ &= \begin{pmatrix} \sum_{i=0}^3 \sum_{j=0}^3 x_{\mu+i, \nu+j} B_i(s) B_j(t) \\ \sum_{i=0}^3 \sum_{j=0}^3 y_{\mu+i, \nu+j} B_i(s) B_j(t) \\ \sum_{i=0}^3 \sum_{j=0}^3 z_{\mu+i, \nu+j} B_i(s) B_j(t) \end{pmatrix}, \quad (2) \end{aligned}$$

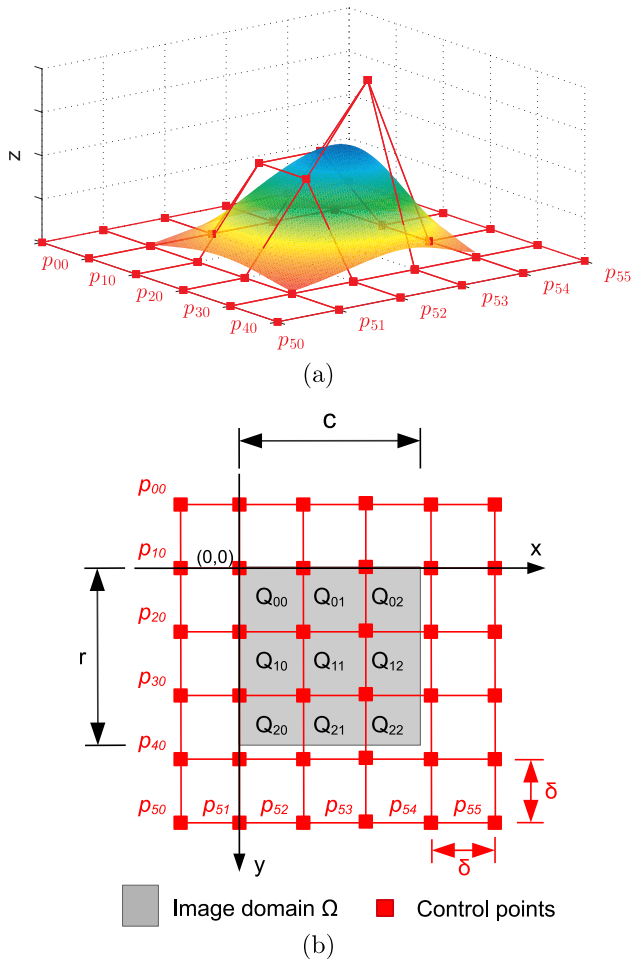


Fig. 1. (a) Example surface with  $3 \times 3$  patches and the corresponding  $6 \times 6$  mesh of control points and (b)  $xy$  plane of the control point grid in (a).

where  $\{\mathbf{p}_{\mu+i,\nu+j} = (x_{\mu+i,\nu+j}, y_{\mu+i,\nu+j}, z_{\mu+i,\nu+j}) | \mu = \lfloor x/\delta \rfloor, \nu = \lfloor y/\delta \rfloor, i, j = 0, 1, 2, 3\}$  are the control points on a  $4 \times 4$  grid that controls the shape of  $\mathbf{Q}_{\mu\nu}$ , and  $B_i(s)$  and  $B_j(t)$  are the  $i$ th and  $j$ th uniform cubic B-spline basis functions evaluated at  $s$  and  $t$ . They are defined as [14,16,17]

$$\begin{aligned} B_0(s) &= (1-s)^3/6, \\ B_1(s) &= (3s^3 - 6s^2 + 4)/6, \\ B_2(s) &= (-3s^3 + 3s^2 + 3s + 1)/6, \\ B_3(s) &= s^3/6. \end{aligned} \quad (3)$$

At an arbitrary pixel position  $(x, y)$ , the displacement  $z$  is computed as

$$z = f(x, y) = \sum_{i=0}^3 \sum_{j=0}^3 z_{\mu+i,\nu+j} B_i(s) B_j(t), \quad (4)$$

where  $z_{\mu+i,\nu+j}$  is the third component of control point  $\mathbf{p}_{\mu+i,\nu+j}$ . Further,  $s = (x/\delta) - \lfloor x/\delta \rfloor$ ,  $t = (y/\delta) - \lfloor y/\delta \rfloor$ ,  $\mu = \lfloor x/\delta \rfloor$ , and  $\nu = \lfloor y/\delta \rfloor$ .

Given this definition, the displacement  $z$  at every location  $(x, y)$  is a weighted combination of the 16 control points in the local neighborhood.

Equation (2) can also be expressed in matrix notation [18]:

$$\begin{aligned} \mathbf{Q}_{\mu\nu} &= \mathbf{s} \mathbf{M} \mathbf{P}_{\mu\nu} \mathbf{M}^T \mathbf{t}^T \\ &= \begin{pmatrix} \mathbf{s} \mathbf{M} \mathbf{X}_{\mu\nu} \mathbf{M}^T \mathbf{t}^T \\ \mathbf{s} \mathbf{M} \mathbf{Y}_{\mu\nu} \mathbf{M}^T \mathbf{t}^T \\ \mathbf{s} \mathbf{M} \mathbf{Z}_{\mu\nu} \mathbf{M}^T \mathbf{t}^T \end{pmatrix}, \end{aligned} \quad (5)$$

where  $\mathbf{s} = [1, s, s^2, s^3]$ ,  $\mathbf{t} = [1, t, t^2, t^3]$ ,  $\mathbf{P}_{\mu\nu} = [\mathbf{p}_{\mu+i,\nu+j}]_{4 \times 4}$ ,  $\mathbf{X}_{\mu\nu} = [x_{\mu+i,\nu+j}]_{4 \times 4}$ ,  $\mathbf{Y}_{\mu\nu} = [y_{\mu+i,\nu+j}]_{4 \times 4}$ ,  $\mathbf{Z}_{\mu\nu} = [z_{\mu+i,\nu+j}]_{4 \times 4}$ ,  $i, j = 0, 1, 2, 3$ , and

$$\mathbf{M} = \frac{1}{6} \begin{bmatrix} 1 & 4 & 1 & 0 \\ -3 & 0 & 3 & 0 \\ 3 & -6 & 3 & 0 \\ -1 & 3 & -3 & 1 \end{bmatrix}. \quad (6)$$

The  $C^2$  continuity of the uniform cubic B-splines guarantees smoothness of the displacement surface formed by individual subsurfaces. Further, due to the local control property of the B-spline model, changing the value of one control point only affects a local surface (the neighboring  $4 \times 4$  subsurfaces) [16,19]. This property allows efficient implementation of multi-level grid refinement (as described in Section 2.B).

## B. Displacement Surface Fitting

The above definitions allow for modeling horizontal and vertical displacements of arbitrary image coordinates. The displacement surface for each image channel is obtained by fitting the previously defined uniform cubic B-spline functions to a set of key-points, which are pixels with known displacement values. The coordinates of these key-points in the (registered and undistorted) reference image  $I_0$  are  $\{(x_{0n}, y_{0n}) \in \Omega | n = 0, 1, \dots, n_k - 1\}$ , with  $n_k$  being the number of key-points. So, again for the case of horizontal displacement, key-points extracted from the uncorrected image  $I$  are defined as  $\mathbf{K} = \{(x_n, y_n, z_n) | z_n = x_{0n} - x_n, n = 0, 1, \dots, n_k - 1\}$  with  $(x_n, y_n)$  being the spatial coordinates of the pixel in  $I$  corresponding to the pixel in  $I_0$  with spatial coordinates  $(x_{0n}, y_{0n})$ , and  $z_n$  being the horizontal displacement value of the key-point. The residual displacement at each key-point location is then defined as the difference between the key-point displacement value and the displacement surface value at the key-point location:

$$\Delta z_n = z_n - f(x_n, y_n), \quad (7)$$

where  $(x_n, y_n, z_n) \in \mathbf{K}$ ,  $f$  is as defined in Eq. (4), and  $n = 0, 1, \dots, n_k - 1$ .

We apply an iterative multilevel refinement of the cubic B-spline model in the fitting process to minimize the residual key-point displacement, leading

to a progressive fit of the displacement surface. The process follows the order depicted in Fig. 2, and is described as follows:

- **Initialization**

A set of 16 control points with zero  $z$  component value are placed on an initial grid of  $4 \times 4$  with spacing  $\delta^{(0)} = 2^{\lceil \log_2 \max\{r,c\} \rceil}$ , with  $r, c$  being the number of rows and columns of the image data. These points control the initial surface  $\mathbf{Q}_{00}$  of size  $\delta^{(0)} \times \delta^{(0)}$ , which is at least equivalent to the size of the image domain  $\Omega$ .

The domain of displacement vector fields is aligned with the upper left corner of  $\mathbf{Q}_{00}$ . In each iteration, the grid spacing is divided by two, resulting in at most  $\log_2(\delta^{(0)})$  refinements steps.

- **Termination condition**

The iterative process terminates under two circumstances. First, if the maximal number of refinement steps  $\log_2(\delta^{(0)})$  is reached, and second, if there is no residual displacement at any key-point location larger than a desired threshold [calculated from Eq. (7)]. In this work, we use one pixel as such.

- **Grid fitting**

The process of grid fitting is that of finding the  $z$  components of the 16 neighboring control points of each subsurface  $\mathbf{Q}_{\mu\nu}$ . These  $z$  components are obtained using a least-square approach that minimizes  $\sum_{i=0}^3 \sum_{j=0}^3 z_{\mu+i, \nu+j}^2$ . The resulting fitted surface then minimizes the deviation of  $f$  in Eq. (4) from zero over the domain  $\Omega$  [17].

We illustrate the calculation of  $z_{ij}^{(l)}$  for an arbitrary control point  $\mathbf{p}_{ij}^{(l)}$  in iteration  $l \times (l = 1, 2, \dots)$ . Let us denote the key-points that are located in the  $4\delta^{(l)} \times 4\delta^{(l)}$  neighborhood of  $\mathbf{p}_{ij}^{(l)}$  as  $\mathbf{K}_{ij}^{(l)} = \{(x_c, y_c, z_c) \in \mathbf{K} | i-2 \leq (x_c/\delta^{(l)}) < i+2, j-2 \leq (y_c/\delta^{(l)}) < j+2\}$ . Control points  $\mathbf{p}_{ij}^{(l)}$  control the subsurfaces in this neighborhood, and key-points  $\mathbf{K}_{ij}^{(l)}$  determine the value of  $\mathbf{p}_{ij}^{(l)}$ . We call  $\mathbf{K}_{ij}^{(l)}$  the proximity key-point set of  $\mathbf{p}_{ij}^{(l)}$ . Correspondingly, the value of  $z_{ij}^{(l)}$  is updated according to the

residual displacement of the key-points in the proximity key-point set  $\mathbf{K}_{ij}$ :

$$z_{ij}^{(l)} = z_{ij}^{(l-1)} + \frac{\sum_c W_c^2 \Delta z'_c}{\sum_c W_c^2}, \quad (8)$$

where  $W_c = B_a(s)B_b(t)$ ,  $a = i + 1 - \lfloor x_c/\delta^{(l)} \rfloor$ ,  $b = j + 1 - \lfloor y_c/\delta^{(l)} \rfloor$ ,  $s = (x_c/\delta^{(l)}) - \lfloor x_c/\delta^{(l)} \rfloor$ ,  $t = (y_c/\delta^{(l)}) - \lfloor y_c/\delta^{(l)} \rfloor$ ,  $(x_c, y_c, z_c) \in \mathbf{K}_{ij}$ , and  $\Delta z'_c$  is defined as

$$\Delta z'_c = \frac{W_c \Delta z_c}{\sum_{k=0}^3 \sum_{l=0}^3 (B_k(s)B_l(t))^2}, \quad (9)$$

where  $\Delta z_c$  is the residual displacement of  $(x_c, y_c, z_c)$  defined in Eq. (7).

- **Grid refinement**

As mentioned above, the grid spacing is halved at each iteration. The refinement is achieved by breaking each parametric range  $s$  and  $t$  at its midpoint and inserting a new control point between each pair of adjacent control points, resulting in a split of each surface into four equal subsurfaces [18,20]. The splitting does not alter the shape of the B-spline surface. As surface  $\mathbf{Q}_{\mu\nu}$  with control points  $\mathbf{P}_{\mu\nu}$  is split into  $\{\mathbf{Q}_{\mu\nu}^{(1)}, \mathbf{Q}_{\mu\nu}^{(2)}, \mathbf{Q}_{\mu\nu}^{(3)}, \mathbf{Q}_{\mu\nu}^{(4)}\}$  (subsurface index from upper-left to lower-right), the parametric cubic B-spline surface function for each subsurface becomes

$$\mathbf{Q}_{\mu\nu}^{(i)} = \mathbf{s} \mathbf{M} \mathbf{P}_{\mu\nu}^{(i)} \mathbf{M}^T \mathbf{t}^T, \quad (10)$$

where  $i = 1, \dots, 4$ . According to [20], the new control points of each subsurface  $\mathbf{P}_{\mu\nu}^{(i)}$  can be computed as  $\mathbf{P}_{\mu\nu}^{(i)} = \alpha_{\text{left}} \mathbf{P}_{\mu\nu} \alpha_{\text{right}}^T$ , given

$$\alpha_{\text{left}} = \begin{cases} A_1 & \text{if } i = 1, 3 \\ A_2 & \text{if } i = 2, 4 \end{cases} \quad \alpha_{\text{right}} = \begin{cases} A_1 & \text{if } i = 1, 2 \\ A_2 & \text{if } i = 3, 4 \end{cases}, \quad (11)$$

$$A_1 = \begin{bmatrix} \frac{1}{2} & \frac{1}{2} & 0 & 0 \\ \frac{1}{8} & \frac{3}{4} & \frac{1}{8} & 0 \\ 0 & \frac{1}{2} & \frac{1}{2} & 0 \\ 0 & \frac{1}{8} & \frac{3}{4} & \frac{1}{8} \end{bmatrix} \quad A_2 = \begin{bmatrix} \frac{1}{8} & \frac{3}{4} & \frac{1}{8} & 0 \\ 0 & \frac{1}{2} & \frac{1}{2} & 0 \\ 0 & \frac{1}{8} & \frac{3}{4} & \frac{1}{8} \\ 0 & 0 & \frac{1}{2} & \frac{1}{2} \end{bmatrix}. \quad (12)$$

Figure 3 shows an example of the grid refinement of surface  $\mathbf{Q}_{00}$ . Before refinement, the surface is controlled by  $4 \times 4$  control points. After refinement, the surface is split into four subsurfaces. Each subsurface is controlled by  $4 \times 4$  control points, and the four subsurfaces together are controlled by  $5 \times 5$  control points.

Not using a fixed number of control points with this multilevel approach allows a high degree of model adaptation to different image sizes and varying degrees of misalignment and distortion.

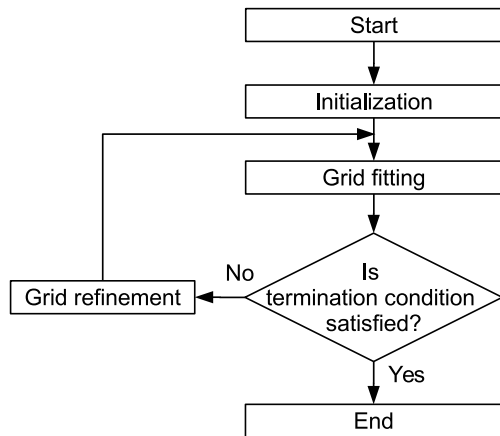
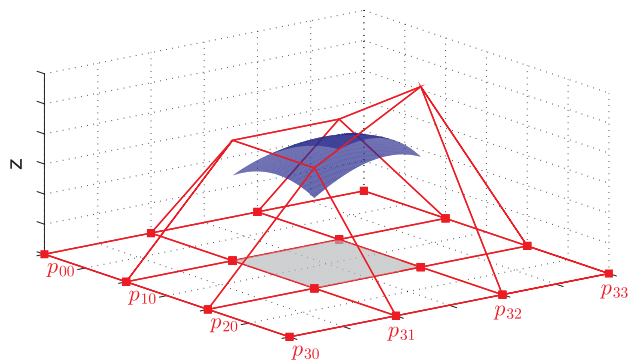
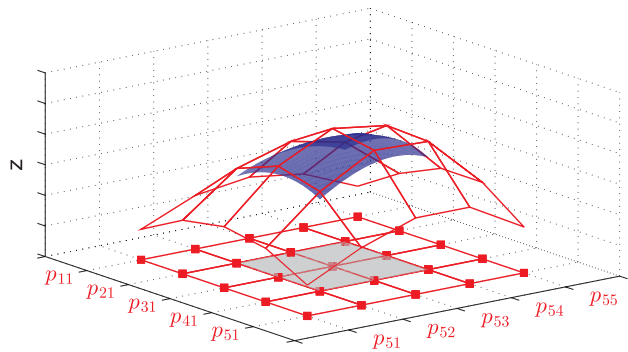


Fig. 2. Flow-chart of the multilevel grid refinement of the uniform cubic B-spline fitting process.



(a) Patch  $Q_{00}$  with  $4 \times 4$  control points.



(b) Patch  $Q_{00}$  after refinement with 4 sub-patches and  $5 \times 5$  control points.

Fig. 3. Example of the multilevel grid refinement process: one refinement step for a sample patch  $Q_{00}$ .

### C. Key-Point Extraction

Key-points are pixels in the image cube with known displacement values (see Section 2.B). Theoretically, key-points can be extracted from arbitrary scene content, as long as the displacement values are known. If spectral image channel registration is to be performed, correspondence of key-points for all spectral images has to be ensured.

We use the spectral scene cube of a printed checkerboard pattern attached to a flat board as the reference object (see Fig. 4, lower left) for key-point extraction. Here, key-points are defined as the corners where checker patches intersect. The Harris corner finder [21] is used to locate the corners in a neighborhood of  $(2/3)d \times (2/3)d$  around an initial position, where  $d$  is the spacing between neighboring black patches. To define the initial positions, four outer corners of black squares are manually selected in the first spectral image  $I_1$  to span a quadrangular region of maximum size. The intermediate initial positions of the other corners in that image are then computed from the four manually selected corners by dividing the quadrangle uniformly in partitions that correspond to the number of vertical and horizontal patches. For the other spectral image channels  $I_\lambda \times (\lambda = 2, 3, \dots, w)$  the initial key-point positions are set to the real key-point positions in  $I_{\lambda-1}$ .

One might ponder locating the corners using the Harris corner finder on the entire image rather than

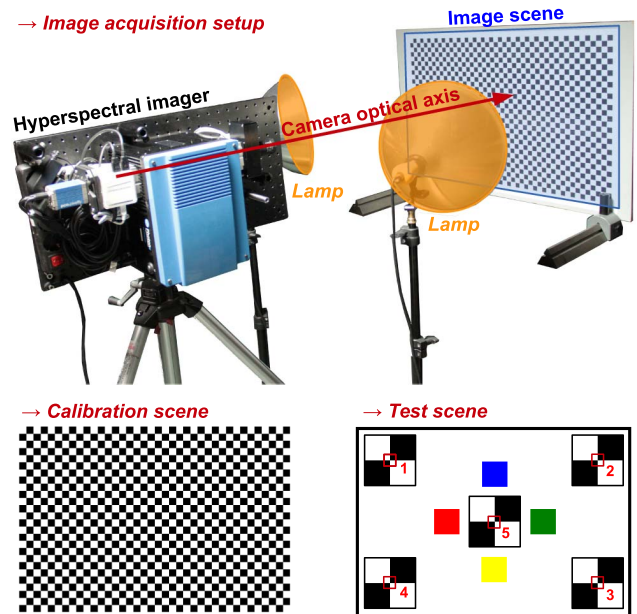


Fig. 4. Illustration of the acquisition setup (up), calibration target (lower left), and test scene (lower right). The numbered red squares in the test scene depict locations (1–5) for which the spectral image channel registration was verified numerically (see Section 3.B).

in a predefined search window as described above. We found this approach to not be very robust to obtain correspondence for corners in all spectral image channels. Locating corners from predefined search windows ensures correspondence and equal numbers of extracted corners in each spectral image channel.

To perform image registration without distortion correction, an arbitrary  $I_\lambda$  can serve as reference image  $I_0$ , to which all other images are registered. If distortion correction is to be performed, the problem occurs that a reference image, free of distortion, is usually not available. However, this limitation can be circumvented in practice for many applications. Recall from Section 2.B that  $I_0$  is not strictly required for displacement surface fitting, but rather the key-point coordinates in  $I_0$ , which are  $\{(x_{0n}, y_{0n}) \in \Omega | n = 0, 1, \dots, n_k - 1\}$ . If the system magnification factor is known and the calibration scene was aligned perpendicular to the optical axis of the system, the checkerboard grid spacing in image pixel units can be determined. Based on the premise that in a distortion-free imaging system the checkerboard pattern is rectilinearly projected, a coordinate grid can be spanned over the image domain. This grid can then be aligned with the calibration scene image data.

### 3. Experiments and Results

In what follows, we introduce the spectral image acquisition device considered in this work. Further, the performance of the proposed approach for image registration and distortion correction is illustrated for several experiments. The spectral image channel registration is verified numerically and by simulating image captures of a conventional RGB camera.

Also, distortion correction is analyzed quantitatively for a test scene.

#### A. Bragg-Grating-Based Hyperspectral Imager

In this study, we have used a volumetric Bragg-grating-based camera (*Hyperspectral Camera V-EOS* by Photon etc. [10]). With this device, spectral data from 400 to 1000 nm can be acquired with a spatial image resolution of  $1392 \times 1040$  pixels. A volumetric Bragg grating is an optical element for which the refraction index varies periodically. The modulation of the refraction index causes light diffraction that affects only a narrow region of the electromagnetic spectrum. Depending on the incidence angle of light and the modulation period of the grating, the element acts as a tunable spectral filter [22–24]. Due to the volumetric nature of the grating, scene radiance from an image scene can be altered such that a spectral filtering occurs in one spatial dimension of the image, whereas the other dimension is not affected. Resulting from that is an image in which the intensity at each pixel is corresponding to a specific spectral part of the scene radiance. The functional behavior of the pixel location and central wavelength of the filter can be obtained in a calibration process (if the incident angle of light on the grating for each image pixel in the scene and the grating modulation frequency are known). By rotating the grating and imposing a modulation of the filter function at each pixel location in the image, it is possible to acquire a set of images that sample the scene radiance with high spectral accuracy. As the functional relation of pixel location and spectral tuning is known, the image cube can be rearranged such that a resulting image cube contains in each channel only the spectral signature of the image content that corresponds to a certain wavelength. The calibration and rectification procedure to obtain a spectral cube is provided by the manufacturer. To achieve the wide spectral range from 400 to 1000 nm, two volumetric gratings with different grating modulation periods are mounted in the device to acquire 400–640 nm and 650–1000 nm, respectively.

In this work, we only used spectral data in the range from 430 to 1000 nm. The reason for this is that in our acquisition configuration, 400–420 nm image channels require very long exposure times and result in generally rather noisy image data that are of less interest for our studies. The scene setup used for this work is illustrated in Fig. 4 and consists of the imaging device and scene illumination from two incandescent light bulbs (Philips PF308) with 500 W each.

When analyzing rectified image cubes after acquisition, the uncorrected image content shows a barrel-shaped distortion pattern at each image channel that is introduced by the optical components of the camera, consisting of a zoom lens, a collimating and focusing lens, various mirrors, and the volumetric Bragg gratings. The distortion effect is further coupled with a wavelength-dependent image misalignment. A sample image of the 700 nm channel

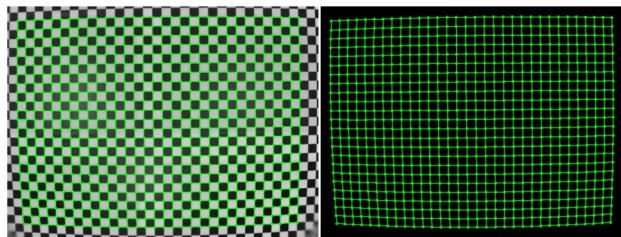


Fig. 5. Key-point extraction for the 700 nm image channel: the left image illustrates the uncorrected calibration scene with an overlay of automatically extracted key-points connected by green lines. In the right image, the extracted key-points are illustrated without the corresponding image.

with the automatically extracted key-point grid is illustrated in Fig. 5. In Fig. 6, the same image scene is illustrated with an overlay of the reference key-point grid in the corresponding reference image.

The illustrated key-points are those visible in all image channels. Key-points close to the edges of the image might not be visible in all image channels or corrupted by noise and are therefore excluded.

#### B. Verifying the Spectral Image Channel Registration Numerically

In a correctly registered image cube, image objects are located at the same spatial position in all spectral image channels. A simple way to verify image registration is therefore to track object points over the spectral dimension of the cube.

For our analysis, we did that for five locations in a specifically designed test scene, illustrated in the lower right of Fig. 4. Locations 1–4 are the intersections of black squared patches close to the image corners, and location 5 is the intersection of black patches in the image center. These corner locations are extracted by applying the automatic corner extraction approach described in Section 2.C. Figure 7 illustrates the x and y coordinates for locations 1–5 and every image channel of the uncorrected and corrected image cube of the test scene.

From this figure, we have some interesting observations. Between the image channels of 640 and 650 nm in the uncorrected cube, a rather large displacement takes place (for instance, for location 1,  $\Delta x = 6.9$  pixels and  $\Delta y = 17.3$  pixels). The misalignment is due to the change in grating that occurs between those channels; i.e., images below 650 nm are acquired using the first grating, and images from

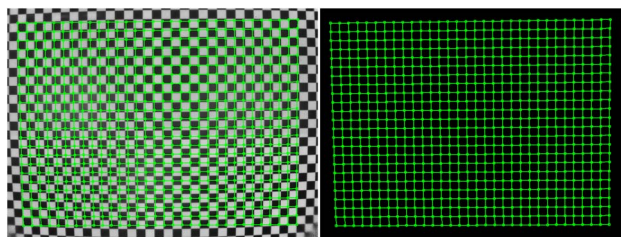


Fig. 6. Sample image of the 700 nm channel with overlay of reference key-points (left) and reference key-points without the corresponding image (right).

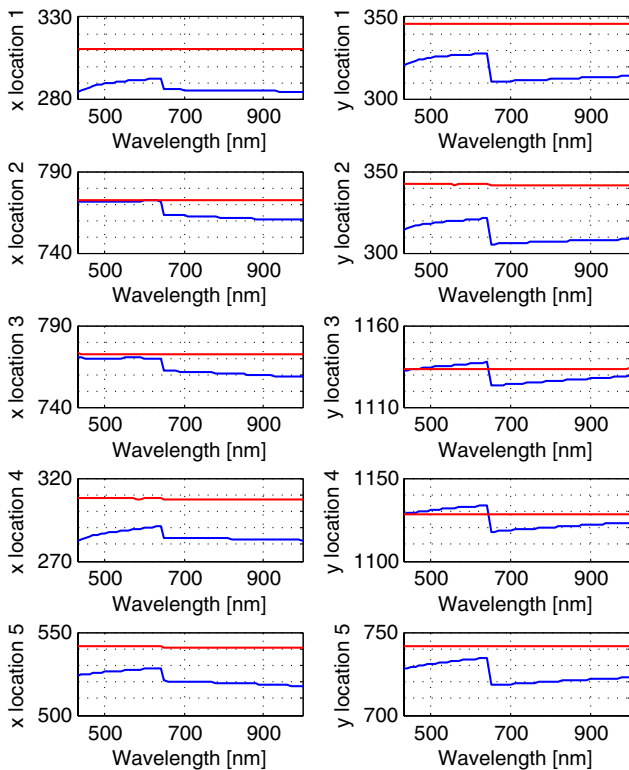


Fig. 7. Locations 1–5 in the test scene (the spatial locations of five center points of the checkerboard pattern) are traced over the spectral dimension. The blue curve illustrates the trace for the uncorrected cube, the red for the corrected cube.

650 nm on are acquired using the second grating. The amount of misalignment due to the different gratings used is expected to be the same at every spatial location in the image. However, when comparing the displacement of location 1 with locations 2–5, it can be observed that the amount of displacement depends on the spatial location (i.e., is different for the five spatial locations). The reason for this is that what is measured from the image is the displacement composed not only by a global translation due to grating misalignment, but also by local distortion of the test scene content.

In summary, from this experiment we can see that the maximal deviation among the selected five locations is reduced from 17 pixels in the uncorrected cube to one pixel in the corrected cube. A significant reduction of misalignment is therefore achieved with the proposed free-form deformation model in all evaluated regions of the test scene.

#### C. Verifying the Spectral Image Channel Registration by Simulated Image Capture

To allow visual assessment of the improvement in image registration, we simulated the capture of a conventional three-channel RGB camera from spectral radiance data. For discrete data, the integral imaging process can be written in matrix form as follows: a camera response at pixel location  $(x,y)$  is simulated as

$$\mathbf{p}_{(x,y)} = \mathbf{Y}\mathbf{r}_{(x,y)}, \quad (13)$$

where  $\mathbf{p}_{(x,y)} \in \mathbb{R}^3$  are camera responses corresponding to radiance  $\mathbf{r}_{(x,y)} \in \mathbb{R}^w$  at spatial location  $(x,y)$ . The  $3 \times w$  matrix of spectral responsivities of the RGB camera system is  $\mathbf{Y}$ , and  $w$  is the dimensionality of spectral data.

In Figs. 8 and 9, the simulated capture of the calibration and test scene is shown for the uncorrected and corrected image cubes. A zoom view is provided for a better illustration of the image quality.

We can see that the color fringe effect, visible in the images rendered from the corrected cubes, is reduced clearly. Another visual effect of the correction is that image sharpness is increased for the corrected image. We measured sharpness from gray-scale images, obtained by transformation of the simulated three-channel  $(R, G, B)$  images using color transformation  $I_{GS} = 0.2989R + 0.5870G + 0.1140B$ . This particular instance of RGB to gray-scale transformation refers to the *rgb2gray* function of the Image Processing Toolbox of the numerical computing environment MATLAB R2012b by MathWorks, Inc. The numerical measure of image sharpness, defined as the sum of the gradient image divided by the number of image pixels, indicates an increase in sharpness of 1.24% over the whole image.

#### D. Verifying the Distortion Correction

As mentioned before, apart from being used to correct channel misalignment, the proposed approach can also correct image distortions at each spectral image channel. Since we could not ensure a perfect perpendicular alignment of the calibration scene with the optical axis of the acquisition system in our setup, we determined an approximation of grid coordinates that served as the reference key-point coordinates  $\{(x_{0n}, y_{0n}) \in \Omega | n = 0, 1, \dots, n_k - 1\}$ . The approximation was achieved by using the manually selected four outer corners in  $I_1$  of the calibration scene and the computed intermediate initial positions of image coordinates where black patches of the checkerboard pattern intersect (see Section 2.C). We have found for our data that this approximation produced satisfactory results.

To assess image distortion, we followed the simple approach of identifying straight lines of scene objects from the image data. Visual assessment of the rendered images of uncorrected and corrected cubes of

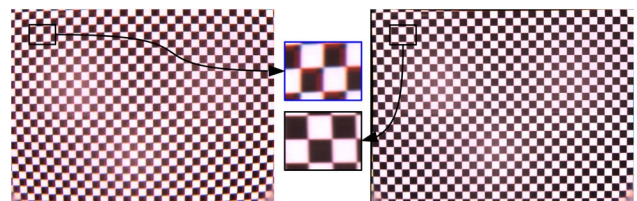


Fig. 8. Color image rendered from the spectral image cube of the calibration scene: before (left) and after (right) correction. The zoom view illustrates the color fringe effect due to channel misalignment.

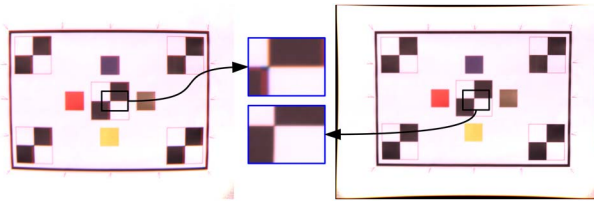


Fig. 9. Color image rendered from the spectral image cube of the test scene: before (left) and after (right) correction. The zoom view illustrates the color fringe effect due to channel misalignment.

the calibration scene in Figs. 8 and 9 illustrates the correction of the barrel-like distortion. The black fringes close to the extremes of the rendered images from corrected cubes (right side in Figs. 8 and 9) correspond to the zero-padding of undefined image coordinates, resulting from the warping process.

Visual assessment is prone to be biased by the subjectivity of the observer, and evaluating the distortion correction on a rendered image does not assure distortion correction at each channel of the image cube. Therefore, we used the black rectangle in the test scene enclosing the checkerboard patterns (see Fig. 4) for a quantitative analysis of distortion.

We defined a measure to characterize the degree of distortion in the test scene. This measure is the relative area difference  $d$ , calculated as

$$d = 100\% \times \left( \frac{A_{\text{real}}}{A_{\text{theo}}} - 1 \right), \quad (14)$$

where  $A_{\text{real}}$  is the area bounded by the distorted rectangle (including the linewidth of the rectangle).  $A_{\text{theo}}$  is the rectangular area enclosed by the four corners of the distorted rectangle.

The distortion measure  $d$  was computed for each image channel of the test scene cube and is illustrated in Fig. 10. From this figure it can be seen that the amount of pixels exceeding the theoretical rectangle size is reduced from approximately 3% in

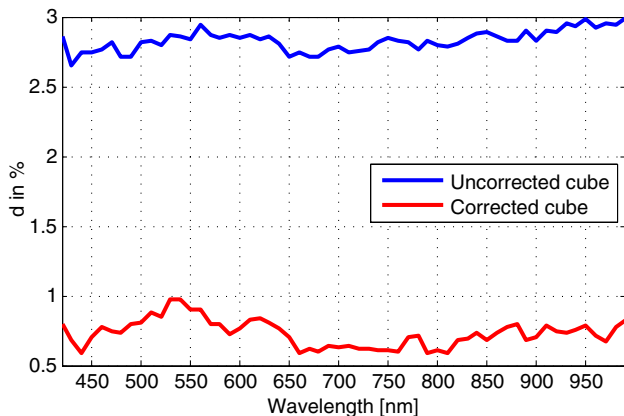


Fig. 10. Amount of distortion  $d$  is quantified for each image channel of the test cube as the relative area difference between the area bounded by the distorted rectangle in the test scene and the rectangular area enclosed by the four corners of the distorted rectangle.

the uncorrected cube to approximately 1% in the corrected cube.

#### 4. Discussion: Comparison with a Related Work

There exists another work about geometric calibration of a spectral imaging system using B-splines by Špiclin *et al.* [15]. Their imaging system captures spectral near-infrared information and is based on an acousto-optic tunable filter and a near-infrared sensitive camera. While the application of their system remains unknown, the description of the optical components indicates acquisition of small objects of approximately  $30 \times 30$  mm, and the spectral range of the acquired data is described to be from 1000 to 1700 nm. The Bragg-grating-based spectral imaging device considered in this work in contrast is sensitive in the visible and the near-infrared range of the electromagnetic spectrum of light (400–1000 nm) and is used for larger scenes. The B-spline model that Špiclin *et al.* use for their system with small FOV only requires a  $4 \times 4 \times 3$  mesh of control points to achieve subpixel accurate image registration, as tested on their corrected calibration scene. This configuration is not accurate enough with our device, as the local image distortion cannot be corrected for at every spatial location in the image with a small number of control points. The multilevel grid refinement that we have used in our approach allows us to obtain subpixel registration accuracy for the calibration scene at any key-point location, and maximum deviation obtained from a test scene of approximately one pixel. Further, in Špiclin *et al.*'s study only a relatively small fraction of image channels from the spectral cube is required to fit the model. The underlying assumption that misalignment and distortion are continuous and smooth over the spectral dimension does not generalize to our device. The mostly automated scheme of key-point extraction and model creation for every image channel presented here, on the other hand, is sufficiently simple to allow modeling image misalignment and distortion for every image channel of the spectral cube.

#### 5. Conclusions

The free-form deformation model of multilevel uniform cubic B-splines seems suitable for channel misalignment and distortion correction of spectral image cubes. It can correct for arbitrary misalignment and distortion patterns. In this work, the model is created empirically by iteratively fitting the multilevel uniform cubic B-spline functions to a set of key-points that are located as scattered data points over the image domain. The multilevel nature of the fitting process makes the model adaptive to image size, degree of misalignment, and degree of distortion, and for some acquisition systems this can be an advantage over the previous study related to hyperspectral image cube registration. For extracting key-points from spectral image data of arbitrary scene content, we have used a semiautomatic method based on the

Harris corner finder that allows subpixel accurate corner extraction in all image channels.

The performance of the proposed approach was evaluated with real image data from a Bragg-grating-based spectral imaging device. The device acquires image data in the visible and near-infrared part of the spectrum of light, and misalignment and distortion occur at all image channels to different degrees. The results of misalignment and distortion correction were evaluated by several measures. First, the image channel misalignment was quantified in different spatial locations of a test scene. For the uncorrected image cube, this residual was found to be up to 17 pixels. For the corrected cube, less than one pixel misalignment was found. Apart from this, RGB color images were rendered from the spectral image cube. Visual assessment indicated that the strong color fringe effect present in the images obtained from uncorrected image cubes vanished entirely. It was shown that the correction also manifests in an increase in image sharpness by 1.17%. To evaluate distortion correction, the deviation of a rectangular image region in the test scene was quantified, and it could be demonstrated that the image distortion can be reduced significantly.

This study was supported by Chromasens GmbH through UGR grant no. 2936, by the Spanish Ministry of Research and Innovation through grant no. DPI2011-23202, and by a joint agreement between Tecnalia Corporation and the Fundacin General UGR-Empresa (reference no. C-3368-00). Our implementation of the B-spline model was inspired by the publicly available MATLAB implementation of B-spline-based image registration (MATLAB Central File-Exchange File ID: #20057) by Dirk-Jan Kroon (University of Twente, The Netherlands).

## References

1. J. Solomon and B. Rock, "Imaging spectrometry for earth remote sensing," *Science* **228**, 1147–1153 (1985).
2. C. Davis, J. Bowles, R. Leathers, D. Korwan, T. Downes, T. Valerie, W. Snyder, W. Rhea, W. Chen, J. Fisher, and P. Bissett, "Ocean PHILLS hyperspectral imager: design, characterization, and calibration," *Opt. Express* **10**, 210–221 (2002).
3. A. Rencz and R. Ryerson, *Manual of Remote Sensing, Remote Sensing for the Earth Sciences* (Wiley, 1999).
4. H. Grahn and P. Geladi, *Techniques and Applications of Hyperspectral Image Analysis* (Wiley, 2007).
5. X. Dai and K. Siamak, "A feature-based image registration algorithm using improved chain-code representation combined with invariant moments," *IEEE Trans. Geosci. Remote Sens.* **37**, 2351–2362 (1999).
6. J. Hardeberg, *Acquisition and Reproduction of Color Images: Colorimetric and Multispectral Approaches* (Dissertation.com, 2001).
7. J. Brauers, N. Schulte, and T. Aach, "Modeling and compensation of geometric distortions of multispectral cameras with optical bandpass filter wheels," in *Proceedings of the 15th European Signal Processing Conference (EUSIPCO)* (2007), Vol. **15**, pp. 1902–1906.
8. D. Foster, K. Amano, S. Nascimento, and M. Foster, "Frequency of metamerism in natural scenes," *J. Opt. Soc. Am. A* **23**, 2359–2372 (2006).
9. D. Gerçek, D. Cesmecı, M. Gullu, M. Kemal, A. Erturk, and S. Erturk, "An automated fine registration of multisensor remote sensing imagery," in *Proceedings of IEEE International Geoscience and Remote Sensing Symposium (IGARSS)* (IEEE, 2012), pp. 1361–1364.
10. Photon etc., "Hyperspectral camera V-EOS," [http://www.photonetc.com/EN/PRODUCTS/Hyperspectral\\_Widefield/HYPERSPECTRAL\\_CAMERA\\_V-EOS](http://www.photonetc.com/EN/PRODUCTS/Hyperspectral_Widefield/HYPERSPECTRAL_CAMERA_V-EOS).
11. D. Brown, "Decentering distortion of lenses," *Photometric Eng.* **32**, 444–462 (1966).
12. J. P. De Villiers, F. W. Leuschner, and R. Geldenhuys, "Centipixel accurate real-time inverse distortion correction," in *International Symposium on Optomechatronic Technologies (SPIE, 2008)*.
13. B. Zitova and J. Flusser, "Image registration methods: a survey," *Image Vis. Comput.* **21**, 977–1000 (2003).
14. C. De Boor, *A Practical Guide to Splines* (Springer-Verlag, 1978).
15. Ž. Špiclin, J. Katrašnik, M. Bürmen, F. Pernuš, and B. Likar, "Geometric calibration of a hyperspectral imaging system," *Appl. Opt.* **49**, 2813–2818 (2010).
16. S. Lee, G. Wolberg, K. Chwa, and S. Shin, "Image metamorphosis with scattered feature constraints," *IEEE Trans. Vis. Comput. Graph.* **2**, 337–354 (1996).
17. S. Lee, G. Wolberg, and S. Shin, "Scattered data interpolation with multilevel B-splines," *IEEE Trans. Vis. Comput. Graph.* **3**, 228–244 (1997).
18. E. Catmull and J. Clark, "Recursively generated B-spline surfaces on arbitrary topological meshes," *Comput. Aided Des.* **10**, 350–355 (1978).
19. D. Rueckert, L. Sonoda, C. Hayes, D. Hill, M. Leach, and D. Hawkes, "Nonrigid registration using free-form deformations: application to breast MR images," *IEEE Trans. Med. Imaging* **18**, 712–721 (1999).
20. D. Forsey and R. Bartels, "Hierarchical B-spline refinement," in *Proceedings of ACM SIGGRAPH Computer Graphics* (ACM, 1998), Vol. **22.4**, pp. 205–212.
21. C. Harris and M. Stephens, "A combined corner and edge detector," in *Proceedings of Alvey Vision Conference* (1988), Vol. **15**, p. 50.
22. S. Blais-Ouellette, O. Daigle, and K. Taylorc, "The imaging Bragg tunable filter," *Proc. SPIE* **6269**, 62695H (2006).
23. S. Blais-Ouellette, E. Wishnow, P. Shopbell, W. van Breugel, K. Taylor, and R. Smith, "Double Bragg grating tunable filter," *Proc. SPIE* **492**, 779–786 (2004).
24. S. Barden, J. Williams, J. Arns, and W. Colburn, "Tunable gratings: imaging the universe in 3-D with volume-phase holographic gratings," in *Imaging the Universe in Three Dimensions* (Citeseer, 2000), Vol. **195**, p. 552.